



Intracellular assembly of supramolecular peptide nanostructures controlled by visible light

Received: 16 September 2024

Accepted: 24 January 2025

Published online: 12 March 2025

Check for updates

Yong Ren¹, Zhixuan Zhou^{1,2}, Iain Harley¹, Özlem Aydin¹, Leon Driehaus-Ortiz¹, Anke Kaltbeitzel¹, Jiaqi Xing¹, Konrad Maxeiner¹, Ingo Lieberwirth¹, Katharina Landfester¹, David Y. W. Ng¹✉ & Tanja Weil¹✉

The complex dynamics of synthetic supramolecular systems in living cellular environments impede the correlation between the transient hierarchical species and their biological functions. Achieving this correlation demands a breakthrough that combines the precise control of supramolecular events at discrete time points via synthetic chemistry with their real-time visualization in native cells. In the present study, we reported two peptide sequences that undergo visible light-induced molecular and supramolecular transformations to form various assembly species in cells. In contrast to endogenous stimulus-responsive assembly, the proposed photochemistry enables full control over the photolysis reaction where the monomer generation and local concentration regulate the subsequent assembly kinetics. Phasor-fluorescence lifetime imaging traced the formation of various assembly states in cells associated with monomer activation and consumption, whereas correlative light-electron microscopy revealed the intracellular nanofibres formed. The temporally resolved assembly process shows that the emergence of cytotoxicity correlates with the accumulation of oligomers beyond the cellular efflux threshold.

Molecular self-assembly plays an indispensable role in cellular life, but the complex dynamics and transience of the diverse supramolecular species within the assembly process impede their structure–activity correlation in biology^{1–9}. In most synthetic systems, precursor molecules undergo defined chemical transformations into active monomers that propagate into various supramolecular intermediates, eventually achieving different nanostructural outcomes. Challenges arise because many parameters such as temperature, lifetime, local concentration of the monomers and intermediates, as well as the nucleation threshold, direct the self-assembly pathways and the subsequent growth of the nanostructure^{10–12}. The heterogeneity of aggregates is further amplified by the formation of kinetically driven, metastable structures on encountering different intracellular environments. Therefore,

synthetic approaches that control the supply of active monomers to produce different assembly states and dynamics is necessary to provide the critical breakthrough in correlating aggregation-based function in living cells.

The control over molecular assemblies is well developed in cell biology, where optogenetic techniques show the transformative use of light to manipulate protein clustering, neuronal function, gene expression and signalling^{13–20}. These seminal studies have inspired us to create a synthetic parallel in which photochemistry is adapted to control supramolecular chemistry and structure formation in living cells. In this respect, photocleavable protecting groups (PPGs) can be designed such that molecules of interest can be released on demand in a spatiotemporal manner, with applications ranging from drug delivery

¹Max Planck Institute for Polymer Research, Mainz, Germany. ²State Key Laboratory of Chemo/Biosensing and Chemometrics, College of Chemistry and Chemical Engineering, Hunan University, Changsha, China. ✉e-mail: david.ng@mpip-mainz.mpg.de; weil@mpip-mainz.mpg.de

to self-healing smart materials^{21,22}. Among various PPGs, coumarin derivatives have been broadly applied as a result of their multifunctional chemical versatility with adaptable wavelengths and tunable photolysis rate²³.

However, in living cells, the selection of a photochemical system is only one of many aspects that dictates the assembly of supramolecular monomers. Depending on the internalization, transport and localization of the molecules, the crowded intracellular environment imposed by the high density of biomacromolecules also influences reaction and assembly kinetics^{24,25}. As these parameters exist only in living cells and cannot be studied in model systems, *in situ* technologies such as the use of phasor-fluorescence lifetime imaging (phasor-FLIM) are invaluable for tracking dynamic self-assembly processes in real time using time-resolved fluorescence²⁶. By combining photocleavable, self-assembling peptides with phasor-FLIM imaging technology, we aim to understand how assembly is controlled, promoted and propagated in living cells.

In the present study, we present the construction of two amphiphilic pro-assembling peptide sequences (**1** and **2**) protected by a visible light-sensitive, coumarin-based photocage. The peptides are designed to undergo visible light-induced molecular and supramolecular transformations to form nanofibres within living cells (Fig. 1). Cell internalization of the caged peptides is facilitated by a cell-penetrating, oligo-arginine peptide sequence. The photolysis reaction and subsequent conversion of the stable photocaged monomers (**1** and **2**) into the ‘active’ self-assembling peptides (**1a** and **2a**) was realized inside living cells on irradiation with 505-nm visible light. In contrast to previously reported caged peptides that respond to endogenous stimuli, such as pH or reactive oxygen species, the irradiation time now controls the uncaging reaction where monomer generation and local concentration regulate the assembly kinetics. A near-infrared (NIR) fluorophore has been attached to peptide **2** to track assembly dynamics, in particular the transition of different molecular and supramolecular species, using the recently reported phasor-FLIM technology. The propagation of these species into nanostructures is subsequently validated by correlative light-electron microscopy (CLEM). We show that an intracellular assembly strategy encoding the molecular information for light sensitivity and fibril formation enables the control and visualization of different assembly states and dynamics of self-assembling peptide monomers, intermediates and nanofibres in living cells. Direct imaging of the complex assembly processes within cells correlates with their impact on cell viability.

Synthesis of the photocaged pro-assembling peptides

The photocleavable pro-assembling peptides (**1** and **2**) have been designed to contain four main functionalities: (1) the self-assembling peptide sequence (Fmoc-Ile-Ser-Val, Fmoc-ISV) carrying (2) the IR780 chromophore as a phasor-FLIM reporter for intracellular imaging of the aggregation process; (3) the red-shifted coumarin photocage that can be cleaved by 505-nm visible light; and (4) a cell-penetrating peptide comprising five arginine (Arg₅) residues, the polarity of which simultaneously prevents assembly and facilitates cellular uptake before irradiation. The design of self-assembling peptide, Fmoc-ISV, is based on short peptide amphiphiles known to assemble into amyloid-like nanostructures^{27,28}. The proposed mechanism involves the initial internalization of the pro-assembling precursors (**1** and **2**) into cells supported by the Arg₅ sequence. In the present study, a co-assembly strategy is essential because **2a**, the photolysis product of precursor **2**, is unable to self-assemble into nanofibres, even at a high concentration of 100 μM (Supplementary Fig. 24). After exposure to 505-nm light, the photocage is cleaved, leading to the release of the active self-assembling monomers (**1a** and **2a**), which co-assemble into NIR-emitting nanofibres. The irradiation time allows control of the generation of the self-assembling monomers (**1a** and **2a**) and their

respective local concentrations. In this way, different assembly states, as well as nanostructure formation, can be regulated within cells.

The synthesis of precursors **1** and **2** involves a combination of solid-phase peptide synthesis (SPPS) and solution-phase methods. The photocage is synthesized in solution through multiple reaction steps (Supplementary Fig. 1a), whereas the peptide components, including Fmoc-ISV and the Arg₅ peptide, are synthesized using SPPS (Supplementary Fig. 1b,c). The conjugate of the photocage and Arg₅ is synthesized in solution via a copper-catalysed azide–alkyne cyclo-addition reaction (Supplementary Fig. 1d), followed by coupling with Fmoc-ISV using diisopropylcarbodiimide and 4-(dimethylamino)-pyridine (Supplementary Fig. 1e). Finally, all protecting groups are cleaved in the presence of 95% trifluoroacetic acid to obtain precursors **1** and **2**, characterized by liquid chromatography–mass spectrometry (LC–MS) and matrix-assisted laser desorption ionization (MALDI)–MS (Supplementary Figs. 20–23). The synthesis details are included in the supporting information (Supplementary Fig. 1).

The photolysis reaction was optimized by LC–MS (Fig. 2b). In NH₄HCO₃ buffer, pH 7.4 (20 mM), precursor **1** remained stable for 24 h in the absence of light (Supplementary Fig. 25). On light irradiation at 505 nm, 9.2 mW cm⁻², the ester bond of **1** (25 μM) was hydrolysed in aqueous buffer (NH₄HCO₃ buffer, pH 7.4, 20 mM), resulting in the formation of self-assembling peptide **1a** and the released photocage–Arg₅ **3**. After 5 min, there was a notable consumption of **1**, accompanied by the emergence of two new peaks with retention times (*t*_R) of 6.91 min and 3.52 min, respectively, both exhibiting *m/z* values consistent with the chemical formula of **1a** (*m/z* = 540.4 for [**1a** + H]⁺ and 562.3 for [**1a** + Na]⁺) and **3** (*m/z* = 636.2 for [**3** + H]²⁺ and 1,270.9 for [**3** + H]⁺) (Fig. 2c). Extending the irradiation time to 20 min leads to a 98% conversion from **1** to **1a** whereas an irradiation of 30 min resulted in the complete disappearance of **1** (Fig. 2b–d). No further discernible effect on the photolysis process was observed if irradiation times were prolonged to 40 and 50 min (Fig. 2b,d). To demonstrate that precursor **2** can also be cleaved by 505-nm light, the corresponding photolysis reaction kinetics were measured. The results indicated that the ester bond of **2** (2.5 μM) was completely hydrolysed within 10 min of irradiation at 505 nm, resulting in the formation of peptide **2a** (Supplementary Fig. 26).

The optical properties associated with the photolysis and self-assembly processes were then investigated. Precursor **1** exhibited an absorption band centred at 505 nm, characteristic of the coumarin chromophore. With increasing irradiation time, the absorption of the coumarin chromophore gradually decreased, accompanied by a slight hypsochromic shift (Fig. 2e). This shift can be attributed to the self-assembly behaviour of **1a** in solution. The emission of the coumarin chromophore on the peptide initially exhibited a slight increase on irradiation, probably as a result of its release from the peptide²⁹. However, this was followed by a gradual decrease, which can be attributed to the self-assembly of **1a** in solution (Fig. 2f).

Light-induced assembly profile and phasor-FLIM calibration

The light-induced self-assembly was initially studied by dynamic light-scattering (DLS) analysis, which featured peptide aggregation over the irradiation times (Fig. 3d). Without irradiation, a 25 μM solution of **1** in phosphate buffer (PB), pH 7.4 (50 mM) remained soluble and exhibited no aggregation (Fig. 3d). After 1 min, nanometre-sized aggregates were already formed that steadily increased and, during the 10 min of irradiation, led to the formation of micrometre-sized aggregates (‘optoaggregates’). The nanostructure and morphology of the optoaggregates were imaged by time-dependent transmission electron microscopy (TEM) using similar irradiation times. Distinct nanofibre structures with increasing fibre densities occurred proportional to the irradiation time. Initially, a small number of fibre fragments were observed after 5 min of irradiation. This was followed by a notable increase in fibre quantity after 15 min of irradiation (Fig. 3a,b).

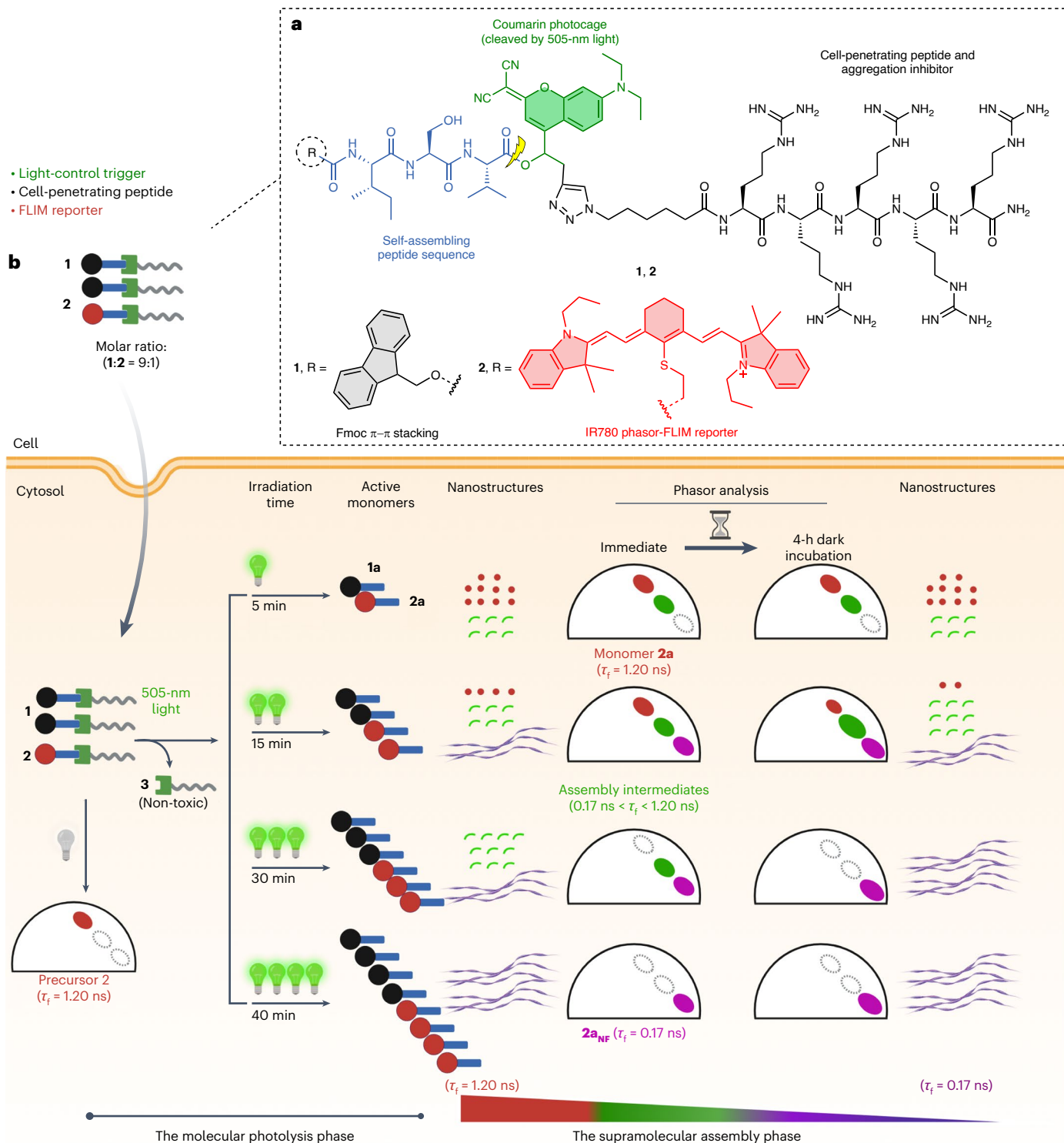


Fig. 1 | Schematic illustration of visible light-triggered intracellular assembly of peptide nanostructures. **a**, Chemical design of the photocaged pro-assembling peptides **1** and **2** in which the formation of intracellular nanofibres can be controlled by light. **b**, Pro-assembling peptides **1** and **2** ($\tau_f = 1.20$ ns) entered A549 cells via ‘Arg_s’-mediated endocytosis. Visible light serves as an external stimulus to transform **1** and **2** into self-assembling peptides **1a** and

2a on irradiation. The irradiation time enables control of the generation and concentration of assembling monomers **1a** and **2a**, which, in turn, regulate the assembly states and dynamics within living cells. The assembly dynamics are monitored as photons change between $\tau_f = 1.20$ ns and $\tau_f = 0.17$ ns during assembly. Figure 1b created with BioRender.com.

With prolonged irradiation to 30 min, the formation of denser nanofibre networks became apparent. Time-dependent, cryogenic, high-resolution TEM images confirmed the formation of similar nanostructures in solution on light exposure (Fig. 3c). Droplet-type

structures that appear at 5 min could possibly hint at the transient presence of liquid–liquid phase separation in the initial stage of assembly³⁰.

Time-dependent circular dichroism (CD) analysis revealed an increasing signal at 203 nm (Fig. 3e), indicating the formation of

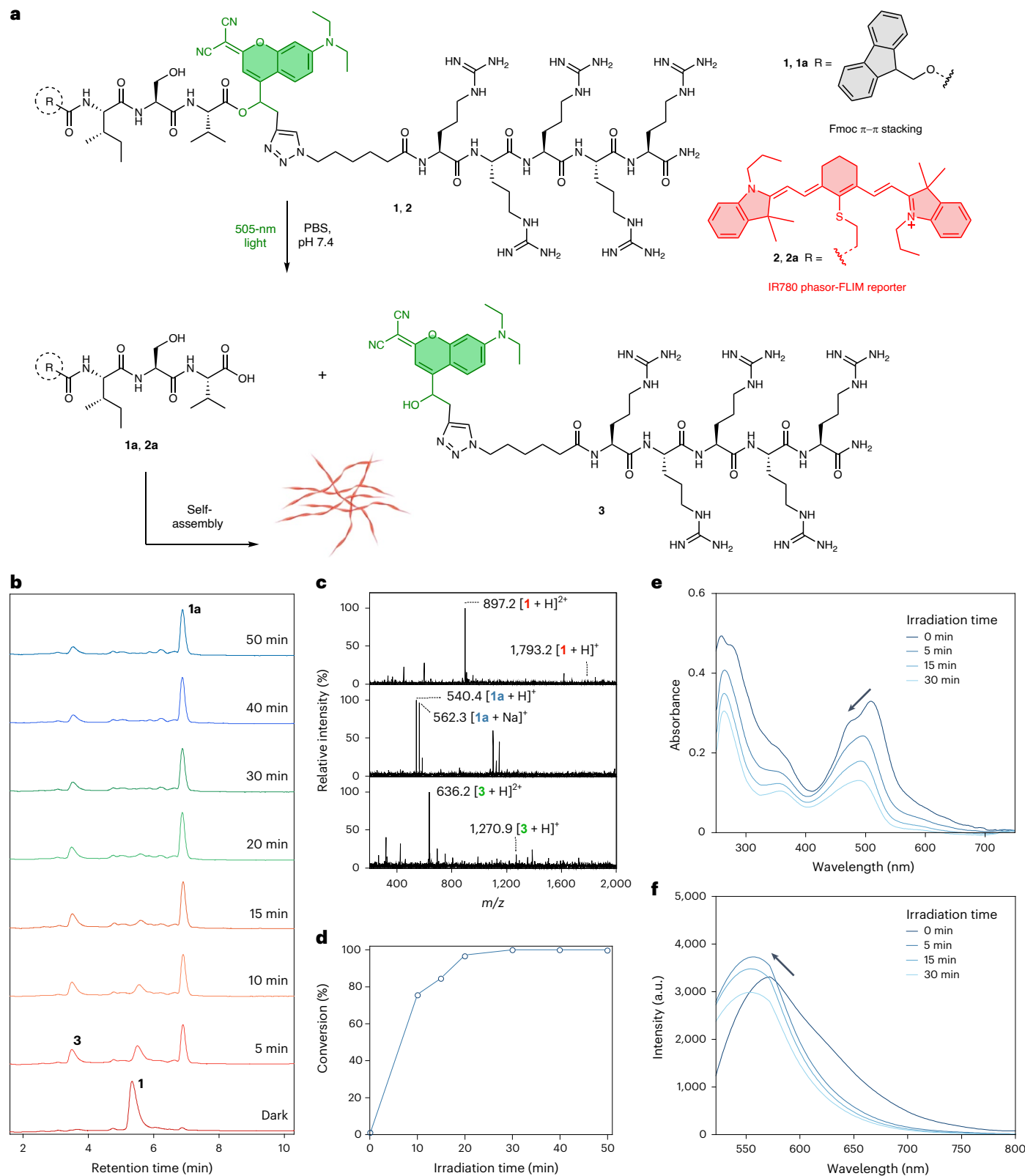


Fig. 2 | Molecular design and kinetic analysis of photolysis reaction.

a, Molecular design and reaction scheme for all chemical transformations of photocaged peptides **1** and **2** (25 μ M, ratio of **1**:**2** = 9:1) that assemble into nanofibres ('optoaggregates'). **b**, LC-MS kinetic analysis for the photolysis reaction of **1** (25 μ M) in NH_4HCO_3 buffer, pH 7.4 (20 mM) on irradiation with 505-nm visible light. **c**, Convoluted MS spectra in the LC-MS analysis for compound **1**.

($t_{\text{R}} = 5.12\text{--}5.73$ min) and corresponding products **1a** ($t_{\text{R}} = 6.73\text{--}7.11$ min) and **3** ($t_{\text{R}} = 3.23\text{--}3.75$ min) after photolysis. **d**, The correlation between light-irradiation time and conversion. The connecting line is drawn only to aid visualization of the trend. **e**, The changes of UV/Vis absorption spectra of **1** (25 μ M) in PB, pH 7.4 (50 mM) after irradiation for 5, 15 or 30 min. **f**, Changes in the fluorescence spectra of **1** (25 μ M) in PB, pH 7.4 (50 mM) after irradiation for 5, 15 or 30 min.

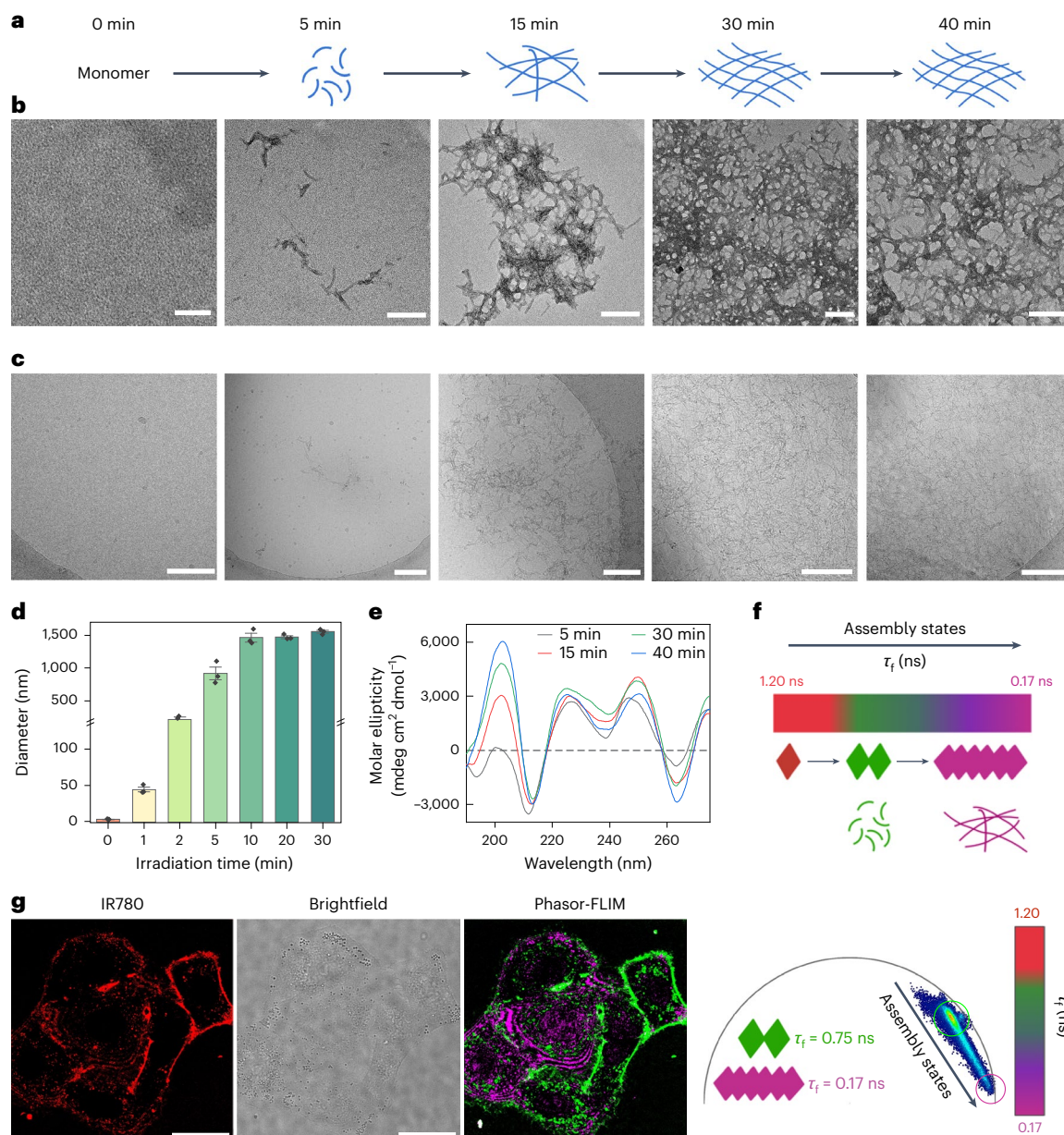


Fig. 3 | Nanofibre formation observed in the light-induced self-assembly over time. **a,b**, Scheme of light-induced peptide assembly (**a**) and corresponding TEM images (**b**) of co-assembled (25 μ M, ratio of **1:2** = 9:1) nanofibres formed at different irradiation times. Scale bar, 200 nm. **c**, Corresponding, cryogenic, high-resolution TEM images of the co-assembled nanofibres (25 μ M) in PB, pH 7.4 (50 mM) over time. Scale bar, 200 nm. **d**, Dynamic light-scattering kinetics analysis for the light-induced nanostructure formation of **1** (25 μ M) in PB, pH 7.4 (50 mM) over time. Changes in diameter were measured. Data are presented as

mean values \pm s.e.m. ($n = 3$, independent experiments). **e**, CD kinetics analysis of **1** in a mixture of PB, pH 7.4 (100 mM) and MeOH (0.5 vol.%) over irradiation time. **f**, Schematic illustration of the assembly dynamics from monomers to assemblies, leading to decreased fluorescence lifetimes (1.20 ns to 0.75 ns to 0.17 ns) on oligomerization and formation of the optoaggregates. **g**, Fluorescence lifetime analysis of assembly progression out of A549 cells using phasor analysis. Two major species can be identified showing τ_f values of 0.75 ns (oligomers) and 0.17 ns (larger assemblies, optoaggregates)

ordered β -sheet secondary structures, which increased during irradiation. In addition, the characteristic $\pi\pi^*$ transition of the Fmoc group at 265 and 274 nm correlated positively with irradiation time, suggesting that the Fmoc group participates in the assembly. However, in the absence of irradiation, precursor **1** showed no obvious signal between 180 nm and 280 nm (Supplementary Fig. 27). To validate the co-assembly behaviour, co-assembled nanofibres (**1a** + **2a**, mol. ratio = 9:1) were prepared in Dulbecco's modified Eagle's medium (DMEM) and imaged using confocal laser-scanning microscopy (CLSM), revealing the presence of NIR-emitting fibres, confirming the successful co-assembly process (Supplementary Fig. 28). To calibrate the fluorescence lifetime profile under physiological conditions, the nanofibres

were assembled in DMEM and transferred on to a culture of A549 lung adenocarcinoma cells. Herein, 0.1 equiv. of peptide **2** with an IR780 dye as a phasor-FLIM reporter was used for co-assembly. The free molecule control was accomplished using non-irradiated **1** + **2** (mol. ratio = 9:1) in A549 cells. Phasor-FLIM analysis revealed that free molecules exhibited a fluorescence lifetime (τ_f) of 1.20 ns before irradiation (Supplementary Fig. 29), whereas the assembled nanofibres revealed a τ_f ranging from 0.75 ns to 0.17 ns, representing different assembly states (Fig. 3f,g).

Visualization of intracellular nanofibre formation
The Arg₅-induced endocytosis into A549 lung alveolar adenocarcinoma cells was visualized using CLSM (Supplementary Fig. 30). Different

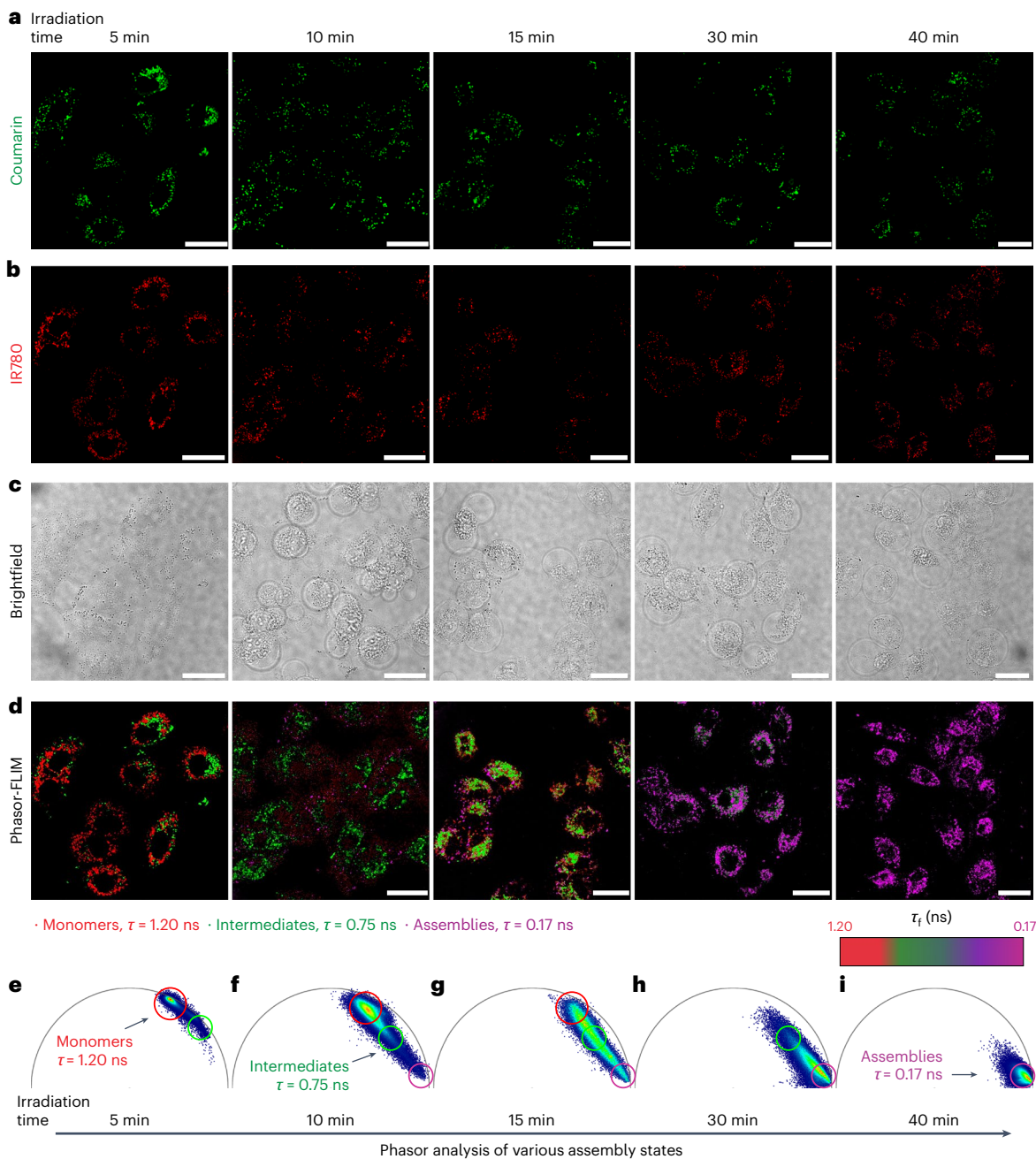


Fig. 4 | Time-lapsed phasor-FLIM analysis of 1 and 2 internalization and assembly states on different irradiation times (505 nm, 9.2 mW cm⁻²). **a–d**, Time-dependent fluorescence of coumarin (**a**) and IR780 (**b**), brightfield (**c**) and phasor-FLIM images (**d**) of A549 cells treated with **1** and **2** (25 μM, ratio of 1:2 = 9:1). **e–i**, Phasor maps of A549 cells treated with **1** and **2** (25 μM, ratio of

1:2 = 9:1) on different irradiation times, including 5 (**e**), 10 (**f**), 15 (**g**), 30 (**h**) and 40 min (**i**). Arrows indicate that the irradiation results in chemical photolysis and the nanostructure formation and growth with a concomitant change in the phasor-FLIM. Scale bars, 25 μm.

incubation times with 25 μM **1 + 2** (mol. ratio = 9:1), ranging from 2 h to 6 h, were tested to determine the optimal conditions for cellular uptake. After 4 h of incubation, peak cellular uptake was observed, as evidenced by both the green fluorescence from the coumarin dye and the NIR emission of IR780 (Supplementary Fig. 30). To acquire an understanding of the assembly progression, we performed corresponding imaging using phasor-FLIM. Cells were pre-treated with **1 + 2** for 4 h, followed by washing off the excess extracellular precursors. Subsequently, the cells were subjected to irradiation (505 nm, 9.2 mW cm⁻²) for 5, 10, 15, 30 and 40 min, followed by immediate phasor-FLIM imaging (Fig. 4d–i).

The progression of aggregation over time can be tracked by the shifting of photon populations between two characteristic phasors on

the phasor plot, representing monomers and assemblies (Fig. 4e–i). In the absence of light, the precursors exhibited a homogeneous, single-component fluorescence decay with $\tau_f = 1.20$ ns (Supplementary Fig. 31). On irradiation, the photocaged peptides (**1** and **2**) generated the corresponding active monomers (**1a** and **2a**), which subsequently self-assembled into nanofibres exhibiting a decreased τ_f . After 5 min of irradiation, the phasor analysis showed intracellular photons exhibiting fluorescence lifetimes of $1.20 \text{ ns} > \tau_f > 0.75 \text{ ns}$, indicating that the major component was still monomers and the first traces of assembled species were observed (Fig. 4e). Supported by TEM and cryo-TEM images, after 5 min of irradiation, only monomers were produced at a low concentration and the formation of oligomers occurred, but no

further progression into mature nanofibres was observed (Fig. 3b,c). When increasing the irradiation time to 10 min, morphological changes of the cells were detected (Fig. 4c) along with the emergence of a new photon population with $\tau_f = 0.17$ ns, indicative of the formation of nanofibres (Fig. 4f). Extending the irradiation time to 15 min led to a further consumption of the generated monomers and the concomitant formation of oligomers and assemblies (Fig. 4g). On 30 min of irradiation, the pool of intracellular precursors was fully consumed and the corresponding population of photons shifting to $\tau_f = 0.17$ ns increased considerably, implying the progression of most supramolecular species into assemblies (Fig. 4h). Finally, irradiation for 40 min resulted in the complete transformation of the photocaged peptides into assemblies (Fig. 4i). With 50% irradiation intensity (4.6 mW cm^{-2}), phasor-FLIM analysis indicated a slower assembly kinetics (Supplementary Fig. 33), where the onset of assembly was shown to require at least 30 min of irradiation. The complete consumption of monomers was observed only after 40 min of irradiation. This observation demonstrated the versatility of the photoresponsive system to regulate the intracellular assembly processes. By correlating IR780 fluorescence to electron microscopy via CLEM, the presence of nanofibres was detected at 15 min of irradiation (505 nm, 9.2 mW cm^{-2}) (Fig. 5 and Supplementary Fig. 39). These nanofibres were found within cytosol and vesicular structures resembling endosomes (Fig. 5b–g), which are in line with the endocytosis process induced by the cell-penetrating peptide³¹.

As irradiation time increased, notable morphological changes in the cells were observed (Fig. 4c). Therefore, a time-dependent cell viability assay was conducted, revealing that 30 min of irradiation in the presence of **1** and **2** reduced cell viability to approximately 37% under these conditions (Supplementary Fig. 32). This suggests that the assembly formation needs to reach a critical point to induce notable cytotoxicity. To rule out the possibility that the cytotoxicity observed was the result of the phototoxicity of 505-nm light, the phototoxic effect of IR780 dye or the byproduct of photolysis, **3**, pertinent experiments were conducted. Initially, phototoxicity from the light source was assessed by conducting cell viability assays and confocal imaging on untreated cells (Supplementary Figs. 34 and 37), revealing that light (505-nm wavelengths, 9.2 mW cm^{-2}) induced minimal toxicity to A549 cells. Furthermore, to investigate the potential cytotoxic effects induced by both the phototoxic effect of IR780 dye and **3**, cell viability was studied on A549 cells treated with **2** at a concentration of $2.5 \mu\text{M}$ used for co-assembly and **3** at $25 \mu\text{M}$ (Supplementary Fig. 37), with and without 30-min irradiation. In addition, confocal imaging was performed for each corresponding treatment (Supplementary Figs. 35 and 36). The results clearly indicated that both compounds did not induce damage to A549 cells (Supplementary Figs. 35–37). Therefore, it can be concluded that the observed cytotoxicity solely resulted from the formation of nanostructures induced by light^{26,32,33}.

Temporal analysis of intracellular nanofibre formation

In contrast to endogenous, stimulus-responsive, self-assembling systems, the light-triggered assembly offers a unique opportunity to control the assembly kinetics within cells by modulating the intracellular concentration of the active monomers. The kinetics involved consist of two distinct phases: the molecular photolysis phase, generating the ‘active’ self-assembling monomers, and the supramolecular assembly phase, during which nuclei are formed that progress to oligomers and mature fibres³⁴. At the molecular level, the photolysis reaction regulates the generation and local concentration of the active monomers that proceed into the self-assembly phase. During assembly, active monomers are consumed relative to their local concentration, which determines the nanostructure formation process. When the local concentration is below the critical aggregation concentration (CAC), assembly does not start and no nanostructures are formed. Conversely, when the concentration of active monomers exceeds

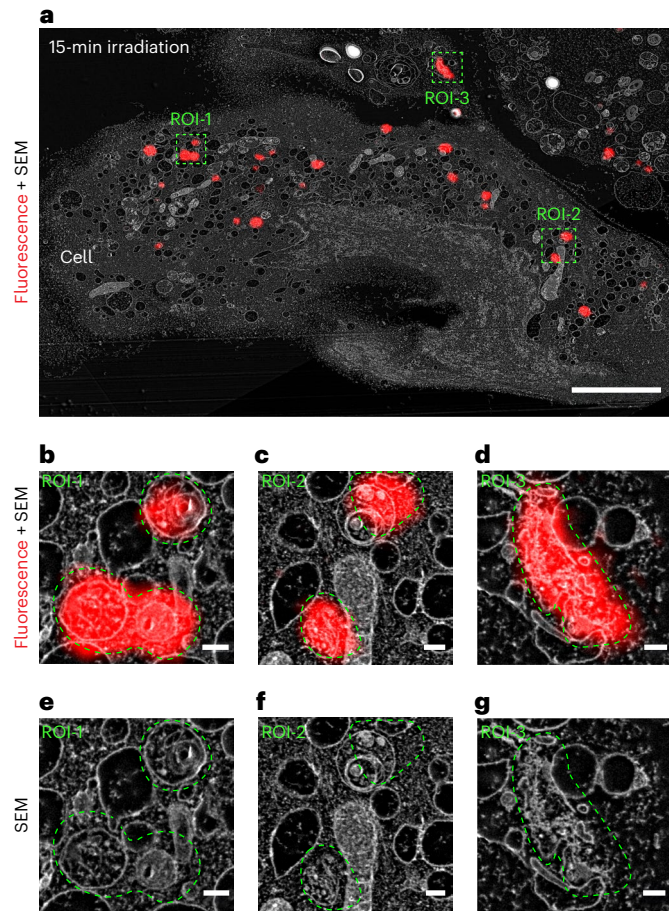


Fig. 5 | CLEM analysis of the formation of nanofibres within A549 cells after 15 min of irradiation (505 nm, 9.2 mW cm^{-2}). a, CLEM-SEM (scanning electron microscopy) micrographs of A549 cells treated for 4 h with **1 + 2** ($25 \mu\text{M}$, 9:1) after 15 min of irradiation, showing the nanostructures of the fibres. Scale bars, $5 \mu\text{m}$. **b,c,d.** Magnified CLEM-SEM micrographs corresponding to region of interest (ROI)-1 (b) (scale bar, 200 nm), ROI-2 (c) (scale bar, 200 nm) and ROI-3 (d) (scale bar, 200 nm). **e,f,g.** Magnified SEM micrographs corresponding to ROI-1 (e) (scale bar, 200 nm), ROI-2 (f) (scale bar, 200 nm) and ROI-3 (g) (scale bar, 200 nm).

the CAC, the production and consumption rates determine the extent of nanostructure formation. If the photolysis production rate of active monomers exceeds their assembly consumption rate, the excess of the active monomers will continue to undergo assembly even after the light has been switched off, causing a loss in temporal precision of the supramolecular polymerization process. To demonstrate these limits, we conducted an extensive analysis of assembly processes and subsequent biological effects on A549 cells (Fig. 6). After identical 4-h peak internalization, the cells were exposed to light for 5, 10, 15 and 30 min, respectively, corresponding to the photolysis conversion of the photocaged precursors (**1** and **2**) in cell-free conditions (Fig. 2d), to control the amount of active monomers that then progressed into the subsequent assembly process. This was followed by a dark incubation period of 1–4 h, during which we examined the assembly progression and the associated biological effects using phasor analysis and cell viability assays (Fig. 6a–h).

With an irradiation time of 5 min, subsequent incubation in the dark for 1–4 h did not show further progression on the phasor plot (Fig. 6a and Supplementary Fig. 40). Phasor analysis revealed that the population of photons remained $1.20 \text{ ns} > \tau_f > 0.75 \text{ ns}$, indicating that the concentration of active monomers surpassed the CAC, therefore leading to nucleation. However, it did not reach a critical concentration threshold for propagation. After irradiation for 10 min, 1-h incubation

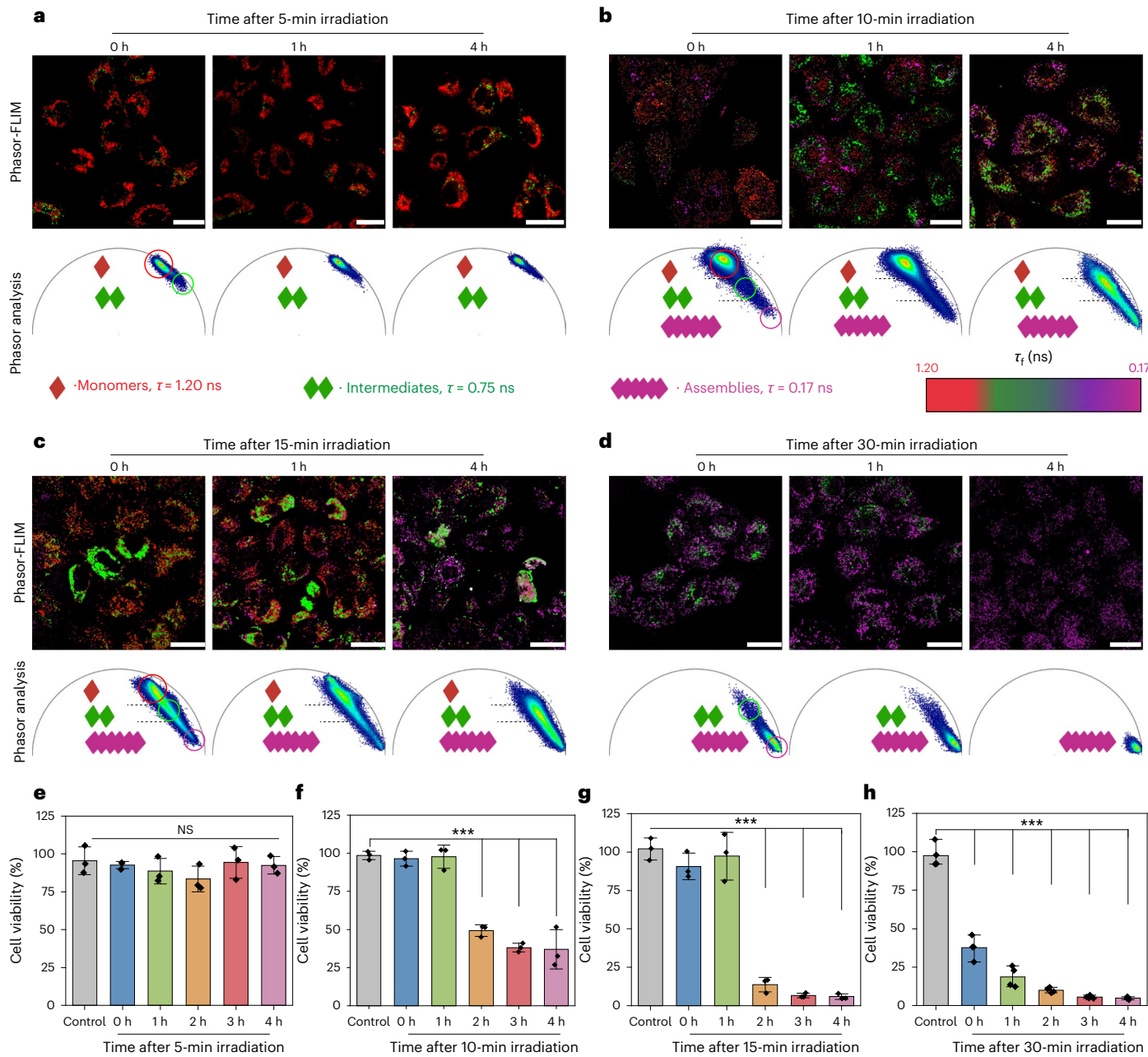


Fig. 6 | Phasor-FLIM analysis and cell viability study of various assembly states and dynamics for 1- to 4-h incubation after different irradiation times (505 nm, 9.2 mW cm⁻²). a–d, Phasor-FLIM analysis of A549 cells for 1- to 4-h incubation after irradiation for 5 (a), 10 (b), 15 (c) and 30 min (d). e–h, Cell viability study for A549 cells for 1- to 4-h incubation after irradiation for 5 (e), 10 (f), 15 (g) and 30 min (h) ($n = 3$, independent experiments (e), $n = 3$, independent experiments (f); $n = 3$, independent experiments (g); $n = 4$, independent experiments (h); scale bars, 25 μ m; $^{\circ}P < 0.001$ versus control (2 h, $P = 1.2 \times 10^{-8}$);

$n = 3$, independent experiments (g); $^{\circ}P < 0.001$ versus control (2 h, $P = 2.9 \times 10^{-7}$, 3 h, $P = 1.8 \times 10^{-7}$, 4 h, $P = 1.7 \times 10^{-7}$); and $n = 4$, independent experiments (h); $^{\circ}P < 0.001$ versus control (0 h, $P = 1.8 \times 10^{-7}$, 1 h, $P = 6.5 \times 10^{-4}$, 2 h, $P = 6.2 \times 10^{-6}$, 3 h, $P = 6.8 \times 10^{-7}$, 4 h, $P = 5 \times 10^{-7}$). NS, not significant. All data are presented as mean \pm s.e.m. Statistical significance was calculated by one-sided ANOVA with Tukey's post hoc test: $^{\circ}P < 0.05$, $^{\circ}P < 0.01$, $^{\circ}P < 0.001$.

in the dark led to an increase in nucleation (Fig. 6b), whereas, after 4 h, most monomers were consumed (Fig. 6b and Supplementary Fig. 41). The results indicated that 10 min of irradiation is sufficient to produce the active monomers in excess which continued to fuel the assembly process even during the dark phase when the light was switched off. Extending the irradiation to 15 min yielded even more noteworthy changes of phasor plots (Fig. 6c and Supplementary Fig. 42). Incubation for 4 h resulted in the increase of the population of photons shifting to $0.75 \text{ ns} > \tau_f > 0.17 \text{ ns}$, indicative of a higher consumption of monomers, further progression into oligomers and the subsequent propagation to nanofibres within the same timeframe.

Furthermore, 30-min irradiation led to complete consumption of the active monomers, with photon populations of $0.75 \text{ ns} > \tau_f > 0.17 \text{ ns}$, corresponding to the formation of a substantial number of assemblies and the presence of a small number of oligomers. Then, 2 h of incubation led to a remarkable increase in assembly propagation and 3-h incubation resulted in the complete transformation of the active

10-min irradiation experiment (Supplementary Fig. 42). Compared with 10-min irradiation, 15-min irradiation generated a considerably higher light-induced uncaging, producing higher monomer concentrations, which further promoted the supramolecular nucleation process and subsequently propagated to nanofibres within the same timeframe.

monomers and oligomers into assemblies (Fig. 6d and Supplementary Fig. 43). The observation indicated that the formation of a substantial amount of assemblies facilitated the propagation of all remaining oligomers, thereby driving the assembly process to completion. Overall, these findings demonstrated that, during assembly, when the photolysis production rate of monomers exceeds their assembly consumption rate, the excess monomers or unconsumed oligomers continue to contribute toward the assembly process even after the cessation of light exposure. In total, our strategy enables effective governance of the molecular photolysis phase to generate accurate concentrations of active monomers that contribute toward the self-assembly phase, which remains unattainable with assembly systems induced by endogenous stimuli. In addition, the photocaged pro-assembling peptides offer a unique opportunity to visualize and unravel supramolecular assembly processes inside living cells, which will be crucial for the formation of artificial nanostructures, compartments or synthetic organelles, an area of emerging importance.

Inspired by the finding that the assembly phase would be continuously fuelled by the overproduction of active monomers, even after the light has been switched off, we hypothesized that associated cytotoxicity caused by the accumulation of oligomers will see a delayed response. To investigate whether the species that were dynamically formed during supramolecular assembly correlate with the corresponding biological effects, cell viability was examined as a function of post-illumination assembly. It is interesting that 5 min of irradiation did not result in toxicity toward A549 cells even after 4 h of incubation (Fig. 6e). However, 10 min of irradiation did not induce toxicity within the first hour of incubation, but resulted in an approximately 50% decrease in cell viability between 2 h and 4 h (Fig. 6f). In addition, 15 min of irradiation resulted in higher toxicity, reducing cell viability to 10% after 2 h (Fig. 6g). After 30 min of light exposure, cell viability immediately decreased to approximately 37%, ultimately dropping to <5% after 4 h (Fig. 6h). By integrating the observed cellular effects with the phasor analysis of the supramolecular assembly processes, it is evident that, during the early stages of assembly, the formation of oligomers does not induce cytotoxicity. However, as these oligomers accumulated and further propagated into larger assemblies, notable cytotoxic effects emerged. These effects are correlated with the quantity of assemblies: specifically, greater numbers of assemblies result in more pronounced cellular toxicity.

Conclusion

We presented photocaged pro-assembling peptides to control and image visible light-induced supramolecular assembly inside complex cellular environments. In combination with imaging technologies, precise control over the generation of diverse assembly states and real-time imaging of these processes was achieved. By integrating imaging and relevant biological assays, we discovered that, during the initial stage of peptide assembly, the formation of oligomers did not lead to observable cytotoxic effects. Notable cytotoxicity was observed only on the formation of sufficient quantities of the supramolecular assemblies. Furthermore, by performing phasor analysis on A549 cells post-irradiation, we elucidated the intricate dynamics of assembly in greater detail in cells. The observation highlighted that the concentration, production rate and consumption rate of monomers substantially influence assembly dynamics inside cells. Although precise control over the molecular phase of photolysis is achievable, managing the supramolecular phase becomes challenging when the production rates of monomers exceed their consumption rates. Time-dependent cell viability analysis revealed that the cytotoxic effects are closely correlated with the quantities of nanostructures formed intracellularly. Our study facilitated precise control over supramolecular events at discrete time points and the imaging technologies offered insights into the dynamic assembly processes with native cells. Our results will pave the way to address challenges in supramolecular drug discovery and relevant biomedical research.

Methods

Chemicals and reagents

Reagents and solvents were purchased from Sigma-Aldrich, TCI and were used without further purification. Peptide synthesis-grade reagents were used for synthesizing the peptides. High-performance liquid chromatography (HPLC) was performed using CH₃CN in HPLC grade (containing 0.1% CF₃COOH) and H₂O for HPLC (containing 0.1% CF₃COOH) and reactions were obtained from a Millipore purification system.

NMR spectroscopy

Nuclear magnetic resonance (NMR) spectra for all compounds and intermediates were recorded on a Bruker Avance III 700-MHz NMR spectrometer. Temperature control was achieved using a VTU (BCU II; variable temperature unit) with an accuracy of $\pm 0.1\text{K}$. The samples were stabilized at the desired temperature for 20 min before the measurements. For ¹H spectra, the chemical shifts were reported in parts per million (ppm) from high to low frequency, using the residual solvent peak as the internal reference (D₂O $\delta = 4.79$ ppm and dimethyl sulfoxide-d6 = 2.50 ppm). All ¹H resonances are reported to the nearest 0.01 ppm. The multiplicity of ¹H signals is indicated as: s, singlet; d, doublet; t, triplet; q, quartet; p, pentet; m, multiplet; br, broad; or combinations thereof. Coupling constants (*J*) were quoted in hertz and reported to the nearest 0.1 Hz. Where appropriate, averages of the signals from peaks displaying multiplicity were used to calculate the value of the coupling constant. Chemical shifts for protons of the compounds were assigned on the basis of COSY and HSQC correlations. The data were processed in MestReNova.

Preparative HPLC

The compounds were purified by preparative HPLC using a setup by Shimadzu. For purification either a ZORBAX Eclipse XDB-C18 HPLC column (9.4 \times 250 mm², 5 μm) was used at a flow rate of 4 ml min⁻¹ or a Phenomenex Gemini 5- μm NX-C18 110 Å (11 nm), 150 \times 30 mm² was used at a flow rate of 25 ml min⁻¹. Experiments were performed using CH₃CN in HPLC grade (containing 0.1% CF₃COOH) and Milli-Q water (containing 0.1% CF₃COOH).

Analytical HPLC

The samples were analysed by analytical HPLC using a setup by Shimadzu. An Atlantis T4 column (4.6 \times 100 mm², 5 μm) was used at a flow rate of 1 ml min⁻¹. Experiments were performed using CH₃CN in HPLC grade (containing 0.1% CF₃COOH) and Milli-Q water (containing 0.1% CF₃COOH). The solvent gradient started with 100% water, then the CH₃CN content was linearly increased to 100% in 20 min. The molar ratio of the compounds was calculated using peak areas at 254 nm. Data were processed in LabSolutions and Origin.

MALDI-TOF-MS

All MALDI-time of flight (MALDI-TOF) spectra were recorded on either a rapifleX MALDI-TOF/TOF from Bruker or MALDI Synapt G2-SI from Waters. Samples were mixed with a saturated solution of the matrix S7 α -cyano-4-hydroxycinnamic acid in NH₄HCO₃ buffer (20 mM):CH₃CN 1:1. Data processing was performed in mMass.

Spectroscopy

The ultraviolet or visible (UV/Vis) absorption spectra for the solutions of the compounds were recorded on a Thermo Fisher Scientific NanoDrop 2000/2000c spectrophotometer in a Hellma high-precision quartz cell, with a 10 \times 10-mm light path. The luminescence emission spectra for the solutions of the compounds were recorded on a Cary Eclipse fluorescence/luminescence spectrophotometer in a Hellma high-precision quartz cell, with a 10 \times 10-mm light path. For the CAC analysis using Nile Red, the luminescence spectra were recorded using a Tecan Spark 20M microplate reader. CD spectra were recorded

on a JASCO J-1500 spectrometer in a Hellma high-precision cell with a 1-mm light path. Data were processed in Spectra Analysis by JASCO and Excel.

Dynamic light scattering

Single-angle DLS measurements were performed at 25 °C using a Malvern ZetaSizer Nano S purchased from Malvern Instruments Ltd with a He/Ne laser ($\lambda = 633$ nm) at a fixed scattering angle of 173°. All measurements were performed in triplicate. The obtained data were processed by cumulant fitting for D_h or CONTIN fitting for intensity-weighted particle-size distribution. Samples were prepared at 25 µM. Dust was removed before each measurement by filtration through GHP syringe filters (0.2-µm pore size, Acrodisc).

Transmission electron microscopy

TEM images of the conjugate solutions were taken on a JEOL 1400 transmission electron microscope at a voltage of 120 kV. Samples were prepared on Formvar- or carbon-film coated copper grids (300 mesh) by Plano GmbH. To prepare the TEM grids, 4 µl of the sample solution was put on freshly glow discharged (30 s at 40 W in a 6:1 oxygen:hydrogen plasma), Formvar-coated copper grids. After 5 min, the solution was removed using a filter paper and grids were stained with 4% uranyl acetate for 2.5 min. The grids were washed 3× with Milli-Q water and dried before measuring. TEM images were processed in ImageJ.

Cryogenic TEM

For cryo-TEM examination, the samples were vitrified using a Vitrobot Mark V (Thermo Fisher Scientific) plunging device. Then, 3 µl of the sample dispersion was applied to a Quantifoil or a lacey, carbon-coated TEM grid that had been glow discharged in a 6:1 oxygen:hydrogen plasma (Diener Nano, Diener electronic) shortly before. After removing excess sample solution with a filter paper, the grid was immediately plunged into liquid ethane. For the subsequent examination the specimen is transferred to a transmission electron microscope (FEI Titan Krios G4), retaining the cryogenic conditions.

Conventional TEM imaging was done using an acceleration voltage of 300 kV. Micrographs were acquired with a 4,000 Direct Electron Detection Camera (Gatan K3) under low-dose conditions.

Cell culture

MDA-MB-231 cells were cultured at 37 °C and 5% CO₂ in DMEM (high glucose), supplemented with 10% fetal bovine serum. Both cell lines were cultured in a T75 culture flask and subcultivated 2–3× per week.

Luminescence detection of cell viability

After performing the CellTiter-Glo Luminescent Cell Viability Assay in a half-area, white, 96-well plate, luminescence intensity was measured on a Promega GloMax-Multi Detection System using the protocol for the CellTiter-Glo Luminescent Cell Viability Assay preinstalled on the instrument. Data were processed in Excel and graphs were generated in Origin.

CLSM and FLIM

CLSM–FLIM imaging was performed on a STELLARIS 8 Leica DMI8 microscope (Leica Microsystems, S/N, 8300000313).

Cells were cultured in an IBIDI 8-well glass-bottomed chamber at a density of 25,000 cells per well in DMEM and allowed to adhere overnight at 37 °C and 5% CO₂. The medium was aspirated and samples pre-dissolved in DMEM at the respective concentrations were introduced into each well. Incubation was performed at 37 °C and 5% CO₂.

Samples were excited using an 80-MHz pulsed, white-light laser tuned to 752 nm for both intensity and fluorescence lifetime measurements. Emitted photons were detected using a HyD X (GaAsP hybrid photocathode) detector with a filter window at 763–835 nm.

FLIM was conducted with fixed cells or living cells, with scanning resolution of 1,024 × 1,024 pixels² at 100 Hz, 2-frame accumulation

equipped with adaptive focusing on each frame and well position. Photons were counted based on a FALCON-modified time-correlated single-photon counting method. Each pixel was transformed into a phasor plot according to the following equation:

$$g_{i,j}(\omega) = \int_0^T I(t) \times \cos(n\omega t) dt / \int_0^T I(t) dt$$

$$s_{i,j}(\omega) = \int_0^T I(t) \times \sin(n\omega t) dt / \int_0^T I(t) dt$$

in which $g_{i,j}(\omega)$ and $s_{i,j}(\omega)$ are the x and y coordinates of the phasor plot, n and ω are the harmonic frequency and the angular frequency of excitation, respectively, and T is the repeat frequency of the acquisition. Frequency domain data acquisition from each pixel can be converted to phasor points using the following transformations:

$$g_{i,j}(\omega) = m_{i,j} \times \cos(\phi_{i,j})$$

$$s_{i,j}(\omega) = m_{i,j} \times \sin(\phi_{i,j})$$

in which $m_{i,j}$ and $\phi_{i,j}$ are the modulation and phase shift, respectively, of the frequency domain measurement at pixel i,j . The decay from each pixel can hence be translated to a point in the phasor plot.

Phasor components were identified and separated using LAS X software. Photons that lie beyond the defined phasor are excluded from the images.

Reporting summary

Further information on research design is available in the Nature Portfolio Reporting Summary linked to this article.

Data availability

The data that support the findings of the present study are available in the text or Supplementary Information and all datasets are available via Zenodo at <https://doi.org/10.5281/zenodo.14627405> (ref. 35). Source data are provided with this paper.

References

- Roth, P. et al. Supramolecular assembly guided by photolytic redox cycling. *Nat. Synth.* **2**, 980–988 (2023).
- Zhou, Z. et al. In situ assembly of platinum(II)-metallopeptide nanostructures disrupts energy homeostasis and cellular metabolism. *J. Am. Chem. Soc.* **144**, 12219–12228 (2022).
- Chagri, S., Ng, D. Y. W. & Weil, T. Designing bioresponsive nanomaterials for intracellular self-assembly. *Nat. Rev. Chem.* **6**, 320–338 (2022).
- Ulijn, R. V. & Smith, A. M. Designing peptide based nanomaterials. *Chem. Soc. Rev.* **37**, 664–675 (2008).
- Lee, S. S. et al. Sulfated glycopeptide nanostructures for multi-potent protein activation. *Nat. Nanotechnol.* **12**, 821–829 (2017).
- Korevaar, P. A. et al. Pathway complexity in supramolecular polymerization. *Nature* **481**, 492–496 (2012).
- Sato, K., Hendricks, M. P., Palmer, L. C. & Stupp, S. I. Peptide supramolecular materials for therapeutics. *Chem. Soc. Rev.* **47**, 7539–7551 (2018).
- Korevaar, P. A., Newcomb, C. J., Meijer, E. W. & Stupp, S. I. Pathway selection in peptide amphiphile assembly. *J. Am. Chem. Soc.* **136**, 8540–8543 (2014).
- Sheehan, F. et al. Peptide-based supramolecular systems chemistry. *Chem. Rev.* **121**, 13869–13914 (2021).
- Zhou, Z., Maxeiner, K., Ng, D. Y. W. & Weil, T. Polymer chemistry in living cells. *Acc. Chem. Res.* **55**, 2998–3009 (2022).
- Jonkheijm, P., van der Schoot, P., Schenning, A. P. H. J. & Meijer, E. W. Probing the solvent-assisted nucleation pathway in chemical self-assembly. *Science* **313**, 80–83 (2006).

12. Ng, D. Y. W. et al. Directing intracellular supramolecular assembly with N-heteroaromatic quaterthiophene analogues. *Nat. Commun.* **8**, 1850 (2017).
13. Shin, Y. et al. Spatiotemporal control of intracellular phase transitions using light-activated optoDroplets. *Cell* **168**, 159–171.e114 (2017).
14. Zhao, E. M. et al. Light-based control of metabolic flux through assembly of synthetic organelles. *Nat. Chem. Biol.* **15**, 589–597 (2019).
15. Emiliani, V. et al. Optogenetics for light control of biological systems. *Nat. Rev. Methods Prim.* **2**, 55 (2022).
16. Gradinaru, V., Mogri, M., Thompson, K. R., Henderson, J. M. & Deisseroth, K. Optical deconstruction of parkinsonian neural circuitry. *Science* **324**, 354–359 (2009).
17. Deisseroth, K. Optogenetics: 10 years of microbial opsins in neuroscience. *Nat. Neurosci.* **18**, 1213–1225 (2015).
18. Mueller, M., Rasoulinejad, S., Garg, S. & Wegner, S. V. The importance of cell-cell interaction dynamics in bottom-up tissue engineering: concepts of colloidal self-assembly in the fabrication of multicellular architectures. *Nano Lett.* **20**, 2257–2263 (2020).
19. Nzigou Mombo, B. et al. Reversible photoregulation of cell-cell adhesions with opto-E-cadherin. *Nat. Commun.* **14**, 6292 (2023).
20. Zhang, A., Zhao, S., Tyson, J., Deisseroth, K. & Bao, Z. Applications of synthetic polymers directed toward living cells. *Nat. Synth.* **3**, 943–957 (2024).
21. Klán, P. et al. Photoremoveable protecting groups in chemistry and biology: reaction mechanisms and efficacy. *Chem. Rev.* **113**, 119–191 (2013).
22. Karimi, M. et al. Smart nanostructures for cargo delivery: uncaging and activating by light. *J. Am. Chem. Soc.* **139**, 4584–4610 (2017).
23. Weinstain, R., Slanina, T., Kand, D. & Klán, P. Visible-to-NIR-light activated release: from small molecules to nanomaterials. *Chem. Rev.* **120**, 13135–13272 (2020).
24. Hansen, M. M. K. et al. Macromolecular crowding creates heterogeneous environments of gene expression in picolitre droplets. *Nat. Nanotechnol.* **11**, 191–197 (2016).
25. Pieszka, M. et al. Controlled supramolecular assembly inside living cells by sequential multistaged chemical reactions. *J. Am. Chem. Soc.* **142**, 15780–15789 (2020).
26. Ren, Y. et al. Supramolecular assembly in live cells mapped by real-time phasor-fluorescence lifetime imaging. *J. Am. Chem. Soc.* **146**, 11991–11999 (2024).
27. Fichman, G. & Gazit, E. Self-assembly of short peptides to form hydrogels: Design of building blocks, physical properties and technological applications. *Acta Biomater.* **10**, 1671–1682 (2014).
28. Frederix, P. W. J. M., Ulijn, R. V., Hunt, N. T. & Tuttle, T. Virtual screening for dipeptide aggregation: toward predictive tools for peptide self-assembly. *J. Phys. Chem. Lett.* **2**, 2380–2384 (2011).
29. Gandioso, A., Cano, M., Massaguer, A. & Marchán, V. A green light-triggerable RGD peptide for photocontrolled targeted drug delivery: synthesis and photolysis studies. *J. Organic Chem.* **81**, 11556–11564 (2016).
30. Yuan, C. et al. Nucleation and growth of amino acid and peptide supramolecular polymers through liquid–liquid phase separation. *Angew. Chem. Int. Ed.* **58**, 18116–18123 (2019).
31. Kondow-McConaghay, H. M. et al. Impact of the endosomal escape activity of cell-penetrating peptides on the endocytic pathway. *ACS Chem. Biol.* **15**, 2355–2363 (2020).
32. Liu, X. et al. In situ self-sorting peptide assemblies in living cells for simultaneous organelle targeting. *J. Am. Chem. Soc.* **144**, 9312–9323 (2022).
33. Liu, X. et al. Apoptosis-amplified assembly of porphyrin nanofiber enhances photodynamic therapy of oral tumor. *J. Am. Chem. Soc.* **145**, 7918–7930 (2023).
34. Yuan, C., Li, Q., Xing, R., Li, J. & Yan, X. Peptide self-assembly through liquid-liquid phase separation. *Chem* **9**, 2425–2445 (2023).
35. Ren, Y. Intracellular assembly of supramolecular peptide nanostructures controlled by visible light. *Zenodo* <https://doi.org/10.5281/zenodo.14627405> (2025).

Acknowledgements

We acknowledge financial support from the Max Planck-Bristol Centre for Minimal Biology and the Deutsche Forschungsgemeinschaft (DFG, German Research Foundation), Projektnummer no. 464588647 (grant no. SFB1551 R04) and Projektnummer no. 213555243 (grant no. SFB 1066 B16). Y.R. and J.X. thank the China Scholarship Council for a fellowship. Z.Z. is supported by the Alexander von Humboldt Foundation.

Author contributions

Y.R., D.Y.W.N. and T.W. conceived the project. Y.R. synthesized the compounds and conducted the TEM, CD analysis and phasor-FLIM imaging experiments. Y.R. and Z.Z. conducted the kinetics analysis. O.A. aided in the synthesis of compounds. J.X. performed the DLS measurement and analysis. Y.R. and K.M. conducted the cellular assay study. I.H., I.L. and K.L. contributed cryo-TEM measurement and analysis. L.D.O. and A.K. conducted the CLEM experiment and data analysis. Y.R. and D.Y.W.N. wrote the manuscript. D.Y.W.N. and T.W. supervised the project and corrected the manuscript. All authors read and approved the final manuscript.

Funding

Open access funding provided by Max Planck Society.

Competing interests

The authors declare no competing interests.

Additional information

Supplementary information The online version contains supplementary material available at <https://doi.org/10.1038/s44160-025-00751-5>.

Correspondence and requests for materials should be addressed to David Y. W. Ng or Tanja Weil.

Peer review information *Nature Synthesis* thanks Jian Ji and the other, anonymous, reviewer(s) for their contribution to the peer review of this work. Primary Handling Editor: Alison Stoddart, in collaboration with the *Nature Synthesis* team.

Reprints and permissions information is available at www.nature.com/reprints.

Publisher's note Springer Nature remains neutral with regard to jurisdictional claims in published maps and institutional affiliations.

Open Access This article is licensed under a Creative Commons Attribution 4.0 International License, which permits use, sharing, adaptation, distribution and reproduction in any medium or format, as long as you give appropriate credit to the original author(s) and the source, provide a link to the Creative Commons licence, and indicate if changes were made. The images or other third party material in this article are included in the article's Creative Commons licence, unless indicated otherwise in a credit line to the material. If material is not included in the article's Creative Commons licence and your intended use is not permitted by statutory regulation or exceeds the permitted use, you will need to obtain permission directly from the copyright holder. To view a copy of this licence, visit <http://creativecommons.org/licenses/by/4.0/>.

Reporting Summary

Nature Research wishes to improve the reproducibility of the work that we publish. This form provides structure for consistency and transparency in reporting. For further information on Nature Research policies, see our [Editorial Policies](#) and the [Editorial Policy Checklist](#).

Statistics

For all statistical analyses, confirm that the following items are present in the figure legend, table legend, main text, or Methods section.

n/a Confirmed

- The exact sample size (n) for each experimental group/condition, given as a discrete number and unit of measurement
- A statement on whether measurements were taken from distinct samples or whether the same sample was measured repeatedly
- The statistical test(s) used AND whether they are one- or two-sided
Only common tests should be described solely by name; describe more complex techniques in the Methods section.
- A description of all covariates tested
- A description of any assumptions or corrections, such as tests of normality and adjustment for multiple comparisons
- A full description of the statistical parameters including central tendency (e.g. means) or other basic estimates (e.g. regression coefficient) AND variation (e.g. standard deviation) or associated estimates of uncertainty (e.g. confidence intervals)
- For null hypothesis testing, the test statistic (e.g. F , t , r) with confidence intervals, effect sizes, degrees of freedom and P value noted
Give P values as exact values whenever suitable.
- For Bayesian analysis, information on the choice of priors and Markov chain Monte Carlo settings
- For hierarchical and complex designs, identification of the appropriate level for tests and full reporting of outcomes
- Estimates of effect sizes (e.g. Cohen's d , Pearson's r), indicating how they were calculated

Our web collection on [statistics for biologists](#) contains articles on many of the points above.

Software and code

Policy information about [availability of computer code](#)

Data collection Leica Microsystems (Leica Stellaris 8, FALCON/DLS), S/N 8300000313

Data analysis ImageJ v1.51a software, Mestra Nova lite V5.2.5-4119 software (mestre lab research S.L.), LAS X

For manuscripts utilizing custom algorithms or software that are central to the research but not yet described in published literature, software must be made available to editors and reviewers. We strongly encourage code deposition in a community repository (e.g. GitHub). See the Nature Research [guidelines for submitting code & software](#) for further information.

Data

Policy information about [availability of data](#)

All manuscripts must include a [data availability statement](#). This statement should provide the following information, where applicable:

- Accession codes, unique identifiers, or web links for publicly available datasets
- A list of figures that have associated raw data
- A description of any restrictions on data availability

The data that support the findings of this study are available in the supporting information and in the Zenodo open access repository (10.5281/zenodo.14627405)

Field-specific reporting

Please select the one below that is the best fit for your research. If you are not sure, read the appropriate sections before making your selection.

- Life sciences Behavioural & social sciences Ecological, evolutionary & environmental sciences

For a reference copy of the document with all sections, see nature.com/documents/hr-reporting-summary-flat.pdf

Life sciences study design

All studies must disclose on these points even when the disclosure is negative.

| | |
|-----------------|---|
| Sample size | No statistical methods were used to determine sample sizes. Sample sizes were determined by allowable error size, accuracy and needed for statistical analysis (all measurements including n >= 3 times independent experiments.) |
| Data exclusions | Exclusions are performed when cells within the well are not confluent (>95%) enough to begin the experiment. |
| Replication | Experiments were repeated at least three independent times with similar results. All experiments were reproduced to reliably support conclusion stated in the manuscript. |
| Randomization | Sample sets are randomly allocated their positions on the 96-well plate. Since only one cell-line is used, there are no further randomization. |
| Blinding | Blinding is not possible in this study because the compounds are intrinsically colored. Investigators therefore know by simply looking at the samples. |

Behavioural & social sciences study design

All studies must disclose on these points even when the disclosure is negative.

| | |
|-------------------|---|
| Study description | Briefly describe the study type including whether data are quantitative, qualitative, or mixed-methods (e.g. qualitative cross-sectional, quantitative experimental, mixed-methods case study). |
| Research sample | State the research sample (e.g. Harvard university undergraduates, villagers in rural India) and provide relevant demographic information (e.g. age, sex) and indicate whether the sample is representative. Provide a rationale for the study sample chosen. For studies involving existing datasets, please describe the dataset and source. |
| Sampling strategy | Describe the sampling procedure (e.g. random, snowball, stratified, convenience). Describe the statistical methods that were used to predetermine sample size OR if no sample-size calculation was performed, describe how sample sizes were chosen and provide a rationale for why these sample sizes are sufficient. For qualitative data, please indicate whether data saturation was considered, and what criteria were used to decide that no further sampling was needed. |
| Data collection | Provide details about the data collection procedure, including the instruments or devices used to record the data (e.g. pen and paper, computer, eye tracker, video or audio equipment) whether anyone was present besides the participant(s) and the researcher, and whether the researcher was blind to experimental condition and/or the study hypothesis during data collection. |
| Timing | Indicate the start and stop dates of data collection. If there is a gap between collection periods, state the dates for each sample cohort. |
| Data exclusions | If no data were excluded from the analyses, state so OR if data were excluded, provide the exact number of exclusions and the rationale behind them, indicating whether exclusion criteria were pre-established. |
| Non-participation | State how many participants dropped out/declined participation and the reason(s) given OR provide response rate OR state that no participants dropped out/declined participation. |
| Randomization | If participants were not allocated into experimental groups, state so OR describe how participants were allocated to groups, and if allocation was not random, describe how covariates were controlled. |

Ecological, evolutionary & environmental sciences study design

All studies must disclose on these points even when the disclosure is negative.

| | |
|-------------------|---|
| Study description | Briefly describe the study. For quantitative data include treatment factors and interactions, design structure (e.g. factorial, nested, hierarchical), nature and number of experimental units and replicates. |
| Research sample | Describe the research sample (e.g. a group of tagged <i>Passer domesticus</i> , all <i>Stenocereus thurberi</i> within Organ Pipe Cactus National Monument), and provide a rationale for the sample choice. When relevant, describe the organism taxa, source, sex, age range and |

any manipulations. State what population the sample is meant to represent when applicable. For studies involving existing datasets, describe the data and its source.

Sampling strategy

Note the sampling procedure. Describe the statistical methods that were used to predetermine sample size OR if no sample-size calculation was performed, describe how sample sizes were chosen and provide a rationale for why these sample sizes are sufficient.

Data collection

Describe the data collection procedure, including who recorded the data and how.

Timing and spatial scale

Indicate the start and stop dates of data collection, noting the frequency and periodicity of sampling and providing a rationale for these choices. If there is a gap between collection periods, state the dates for each sample cohort. Specify the spatial scale from which the data are taken.

Data exclusions

If no data were excluded from the analyses, state so OR if data were excluded, describe the exclusions and the rationale behind them, indicating whether exclusion criteria were pre-established.

Reproducibility

Describe the measures taken to verify the reproducibility of experimental findings. For each experiment, note whether any attempts to repeat the experiment failed OR state that all attempts to repeat the experiment were successful.

Randomization

Describe how samples/organisms/participants were allocated into groups. If allocation was not random, describe how covariates were controlled. If this is not relevant to your study, explain why.

Blinding

Describe the extent of blinding used during data acquisition and analysis. If blinding was not possible, describe why OR explain why blinding was not relevant to your study.

Did the study involve field work? Yes No

Field work, collection and transport

Field conditions

Describe the study conditions for field work, providing relevant parameters (e.g. temperature, rainfall).

Location

State the location of the sampling or experiment, providing relevant parameters (e.g. latitude and longitude, elevation, water depth).

Access & import/export

Describe the efforts you have made to access habitats and to collect and import/export your samples in a responsible manner and in compliance with local, national and international laws, noting any permits that were obtained (give the name of the issuing authority, the date of issue, and any identifying information).

Disturbance

Describe any disturbance caused by the study and how it was minimized.

Reporting for specific materials, systems and methods

We require information from authors about some types of materials, experimental systems and methods used in many studies. Here, indicate whether each material, system or method listed is relevant to your study. If you are not sure if a list item applies to your research, read the appropriate section before selecting a response.

Materials & experimental systems

- | | |
|-------------------------------------|---|
| n/a | Involved in the study |
| <input checked="" type="checkbox"/> | <input type="checkbox"/> Antibodies |
| <input type="checkbox"/> | <input checked="" type="checkbox"/> Eukaryotic cell lines |
| <input checked="" type="checkbox"/> | <input type="checkbox"/> Palaeontology and archaeology |
| <input checked="" type="checkbox"/> | <input type="checkbox"/> Animals and other organisms |
| <input checked="" type="checkbox"/> | <input type="checkbox"/> Human research participants |
| <input checked="" type="checkbox"/> | <input type="checkbox"/> Clinical data |
| <input checked="" type="checkbox"/> | <input type="checkbox"/> Dual use research of concern |

Methods

- | | |
|-------------------------------------|---|
| n/a | Involved in the study |
| <input checked="" type="checkbox"/> | <input type="checkbox"/> ChIP-seq |
| <input checked="" type="checkbox"/> | <input type="checkbox"/> Flow cytometry |
| <input checked="" type="checkbox"/> | <input type="checkbox"/> MRI-based neuroimaging |

Antibodies

Antibodies used

Describe all antibodies used in the study; as applicable, provide supplier name, catalog number, clone name, and lot number.

Validation

Describe the validation of each primary antibody for the species and application, noting any validation statements on the manufacturer's website, relevant citations, antibody profiles in online databases, or data provided in the manuscript.

Eukaryotic cell lines

Policy information about [cell lines](#)

Cell line source(s)

A549 cell line was purchased from American Type Culture Collection (ATCC)

| | |
|--|--|
| Authentication | Authenticated by Short Tandem Repeat Profiling from ATCC when bought. Passages used for experiments are between 3 to 10. |
| Mycoplasma contamination | Certified free of Mycoplasma contamination when bought. No further tests for Mycoplasma. |
| Commonly misidentified lines (See ICLAC register) | Cell line used in the study are not within the commonly misidentified lines |

Palaeontology and Archaeology

| | |
|---|--|
| Specimen provenance | <i>Provide provenance information for specimens and describe permits that were obtained for the work (including the name of the issuing authority, the date of issue, and any identifying information).</i> |
| Specimen deposition | <i>Indicate where the specimens have been deposited to permit free access by other researchers.</i> |
| Dating methods | <i>If new dates are provided, describe how they were obtained (e.g. collection, storage, sample pretreatment and measurement), where they were obtained (i.e. lab name), the calibration program and the protocol for quality assurance OR state that no new dates are provided.</i> |
| <input type="checkbox"/> Tick this box to confirm that the raw and calibrated dates are available in the paper or in Supplementary Information. | |
| Ethics oversight | <i>Identify the organization(s) that approved or provided guidance on the study protocol, OR state that no ethical approval or guidance was required and explain why not.</i> |

Note that full information on the approval of the study protocol must also be provided in the manuscript.

Animals and other organisms

Policy information about [studies involving animals; ARRIVE guidelines](#) recommended for reporting animal research

| | |
|-------------------------|---|
| Laboratory animals | <i>For laboratory animals, report species, strain, sex and age OR state that the study did not involve laboratory animals.</i> |
| Wild animals | <i>Provide details on animals observed in or captured in the field; report species, sex and age where possible. Describe how animals were caught and transported and what happened to captive animals after the study (if killed, explain why and describe method; if released, say where and when) OR state that the study did not involve wild animals.</i> |
| Field-collected samples | <i>For laboratory work with field-collected samples, describe all relevant parameters such as housing, maintenance, temperature, photoperiod and end-of-experiment protocol OR state that the study did not involve samples collected from the field.</i> |
| Ethics oversight | <i>Identify the organization(s) that approved or provided guidance on the study protocol, OR state that no ethical approval or guidance was required and explain why not.</i> |

Note that full information on the approval of the study protocol must also be provided in the manuscript.

Human research participants

Policy information about [studies involving human research participants](#)

| | |
|----------------------------|--|
| Population characteristics | <i>Describe the covariate-relevant population characteristics of the human research participants (e.g. age, gender, genotypic information, past and current diagnosis and treatment categories). If you filled out the behavioural & social sciences study design questions and have nothing to add here, write "See above."</i> |
| Recruitment | <i>Describe how participants were recruited. Outline any potential self-selection bias or other biases that may be present and how these are likely to impact results.</i> |
| Ethics oversight | <i>Identify the organization(s) that approved the study protocol.</i> |

Note that full information on the approval of the study protocol must also be provided in the manuscript.

Clinical data

Policy information about [clinical studies](#)

All manuscripts should comply with the ICMJE [guidelines for publication of clinical research](#) and a completed [CONSORT checklist](#) must be included with all submissions.

| | |
|-----------------------------|--|
| Clinical trial registration | <i>Provide the trial registration number from ClinicalTrials.gov or an equivalent agency.</i> |
| Study protocol | <i>Note where the full trial protocol can be accessed OR if not available, explain why.</i> |
| Data collection | <i>Describe the settings and locales of data collection, noting the time periods of recruitment and data collection.</i> |
| Outcomes | <i>Describe how you pre-defined primary and secondary outcome measures and how you assessed these measures.</i> |

Dual use research of concern

Policy information about [dual use research of concern](#)

Hazards

Could the accidental, deliberate or reckless misuse of agents or technologies generated in the work, or the application of information presented in the manuscript, pose a threat to:

- | | |
|--------------------------|---|
| No | Yes |
| <input type="checkbox"/> | <input type="checkbox"/> Public health |
| <input type="checkbox"/> | <input type="checkbox"/> National security |
| <input type="checkbox"/> | <input type="checkbox"/> Crops and/or livestock |
| <input type="checkbox"/> | <input type="checkbox"/> Ecosystems |
| <input type="checkbox"/> | <input type="checkbox"/> Any other significant area |

Experiments of concern

Does the work involve any of these experiments of concern:

- | | |
|--------------------------|--|
| No | Yes |
| <input type="checkbox"/> | <input type="checkbox"/> Demonstrate how to render a vaccine ineffective |
| <input type="checkbox"/> | <input type="checkbox"/> Confer resistance to therapeutically useful antibiotics or antiviral agents |
| <input type="checkbox"/> | <input type="checkbox"/> Enhance the virulence of a pathogen or render a nonpathogen virulent |
| <input type="checkbox"/> | <input type="checkbox"/> Increase transmissibility of a pathogen |
| <input type="checkbox"/> | <input type="checkbox"/> Alter the host range of a pathogen |
| <input type="checkbox"/> | <input type="checkbox"/> Enable evasion of diagnostic/detection modalities |
| <input type="checkbox"/> | <input type="checkbox"/> Enable the weaponization of a biological agent or toxin |
| <input type="checkbox"/> | <input type="checkbox"/> Any other potentially harmful combination of experiments and agents |

ChIP-seq

Data deposition

- Confirm that both raw and final processed data have been deposited in a public database such as [GEO](#).
- Confirm that you have deposited or provided access to graph files (e.g. BED files) for the called peaks.

Data access links

May remain private before publication.

For "Initial submission" or "Revised version" documents, provide reviewer access links. For your "Final submission" document, provide a link to the deposited data.

Files in database submission

Provide a list of all files available in the database submission.

Genome browser session (e.g. [UCSC](#))

Provide a link to an anonymized genome browser session for "Initial submission" and "Revised version" documents only, to enable peer review. Write "no longer applicable" for "Final submission" documents.

Methodology

Replicates

Describe the experimental replicates, specifying number, type and replicate agreement.

Sequencing depth

Describe the sequencing depth for each experiment, providing the total number of reads, uniquely mapped reads, length of reads and whether they were paired- or single-end.

Antibodies

Describe the antibodies used for the ChIP-seq experiments; as applicable, provide supplier name, catalog number, clone name, and lot number.

Peak calling parameters

Specify the command line program and parameters used for read mapping and peak calling, including the ChIP, control and index files used.

Data quality

Describe the methods used to ensure data quality in full detail, including how many peaks are at FDR 5% and above 5-fold enrichment.

Software

Describe the software used to collect and analyze the ChIP-seq data. For custom code that has been deposited into a community repository, provide accession details.

Flow Cytometry

Plots

Confirm that:

- The axis labels state the marker and fluorochrome used (e.g. CD4-FITC).
- The axis scales are clearly visible. Include numbers along axes only for bottom left plot of group (a 'group' is an analysis of identical markers).
- All plots are contour plots with outliers or pseudocolor plots.
- A numerical value for number of cells or percentage (with statistics) is provided.

Methodology

Sample preparation

Describe the sample preparation, detailing the biological source of the cells and any tissue processing steps used.

Instrument

Identify the instrument used for data collection, specifying make and model number.

Software

Describe the software used to collect and analyze the flow cytometry data. For custom code that has been deposited into a community repository, provide accession details.

Cell population abundance

Describe the abundance of the relevant cell populations within post-sort fractions, providing details on the purity of the samples and how it was determined.

Gating strategy

Describe the gating strategy used for all relevant experiments, specifying the preliminary FSC/SSC gates of the starting cell population, indicating where boundaries between "positive" and "negative" staining cell populations are defined.

- Tick this box to confirm that a figure exemplifying the gating strategy is provided in the Supplementary Information.

Magnetic resonance imaging

Experimental design

Design type

Indicate task or resting state; event-related or block design.

Design specifications

Specify the number of blocks, trials or experimental units per session and/or subject, and specify the length of each trial or block (if trials are blocked) and interval between trials.

Behavioral performance measures

State number and/or type of variables recorded (e.g. correct button press, response time) and what statistics were used to establish that the subjects were performing the task as expected (e.g. mean, range, and/or standard deviation across subjects).

Acquisition

Imaging type(s)

Specify: functional, structural, diffusion, perfusion.

Field strength

Specify in Tesla

Sequence & imaging parameters

Specify the pulse sequence type (gradient echo, spin echo, etc.), imaging type (EPI, spiral, etc.), field of view, matrix size, slice thickness, orientation and TE/TR/flip angle.

Area of acquisition

State whether a whole brain scan was used OR define the area of acquisition, describing how the region was determined.

Diffusion MRI

Used

Not used

Preprocessing

Preprocessing software

Provide detail on software version and revision number and on specific parameters (model/functions, brain extraction, segmentation, smoothing kernel size, etc.).

Normalization

If data were normalized/standardized, describe the approach(es): specify linear or non-linear and define image types used for transformation OR indicate that data were not normalized and explain rationale for lack of normalization.

Normalization template

Describe the template used for normalization/transformation, specifying subject space or group standardized space (e.g. original Talairach, MNI305, ICBM152) OR indicate that the data were not normalized.

Noise and artifact removal

Describe your procedure(s) for artifact and structured noise removal, specifying motion parameters, tissue signals and physiological signals (heart rate, respiration).

Volume censoring

Define your software and/or method and criteria for volume censoring, and state the extent of such censoring.

Statistical modeling & inference**Model type and settings**

Specify type (mass univariate, multivariate, RSA, predictive, etc.) and describe essential details of the model at the first and second levels (e.g. fixed, random or mixed effects; drift or auto-correlation).

Effect(s) tested

Define precise effect in terms of the task or stimulus conditions instead of psychological concepts and indicate whether ANOVA or factorial designs were used.

Specify type of analysis: Whole brain ROI-based Both

**Statistic type for inference
(See Eklund et al. 2016)**

Specify voxel-wise or cluster-wise and report all relevant parameters for cluster-wise methods.

Correction

Describe the type of correction and how it is obtained for multiple comparisons (e.g. FWE, FDR, permutation or Monte Carlo).

Models & analysis**n/a** Involved in the study

- Functional and/or effective connectivity
- Graph analysis
- Multivariate modeling or predictive analysis

Functional and/or effective connectivity

Report the measures of dependence used and the model details (e.g. Pearson correlation, partial correlation, mutual information).

Graph analysis

Report the dependent variable and connectivity measure, specifying weighted graph or binarized graph, subject- or group-level, and the global and/or node summaries used (e.g. clustering coefficient, efficiency, etc.).

Multivariate modeling and predictive analysis

Specify independent variables, features extraction and dimension reduction, model, training and evaluation metrics.